J Mater Sci: Mater Electron

Electrical studies on a single, binary, and ternary nanocomposites of Mn_3O_4@TiO_2@rGO

M. El-Shahat[1], M. Mokhtar[1], M. M. Rashad[2], and M. A. Mousa[1,*]

[1] Chemistry Department, Faculty of Science, Benha University, Benha, Egypt
[2] Central Metallurgical Research and Development Institute, Cairo, Helwan, Egypt

Received: 8 January 2021
Accepted: 3 March 2021

ABSTRACT

The present work is concerned with studying the electrical and dielectric properties of a single, binary, and ternary nanocomposite of Mn_3O_4 (M), TiO_2 (T), and reduced graphene oxide (RGO). The electrical properties of the investigated systems were studied via dc-, ac- conductivity, dielectric, and impedance spectroscopy (EIS) measurements. The electrical conductivity is found to increase in the following order: rGO > T@rGO > Ti > M@rGO > M@T > M@T@rGO > M. The dielectric constant (ε') and dielectric losses (ε'') values of all materials showed a monotonous decrease with an exponential behavior by increasing the applied ac. Frequency. At constant frequency and temperature, the ε' value followed the order: TiO_2 > rGO > T@rGO > M@rGO > M@T > M@T@rGO > M, whereas, the ε'' value followed the order: T@rGO > T > rGO > M@rGO > M@T > M@T@rGO > M. The results obtained were explained and discussed.

1 Introduction

At present, there has been a great interest in metal oxide nanoparticles because of their special electronic structure, physical, chemical, and structural features. Their features extend from insulating to semiconductors and conductors. The variety of their applications derives from the more complicated crystal structure, morphology, and electronic configurations compared to other materials. The scope of metal oxides is very big, but is stretched even more by studying binary and more complicated structures, where extra attractive properties are existent. From the category of metal oxides are the 3d transition metal oxides (TMO) for example manganese oxides, which have drawn significant interest because of their potential uses in several fields. Mn_3O_4 is one of the most stable mixed oxides in which Mn exists in several oxidation states ($Mn^{2+}(Mn^{3+})_2O_4$) with spinel structure. Although the number of research works reported to Mn_3O_4 is not as much of MnO_2 and MnO, it has in recent times derived growing attention in technological applications [1]. Nanoscale Mn_3O_4 materials with different morphological structures and significant specific surface areas are of major attention for investigators from a wide range of disciplines. Nanosized Mn_3O_4 has been broadly

Address correspondence to E-mail: mousa_chem@yahoo.com

https://doi.org/10.1007/s10854-021-05678-z
Published online: 20 March 2021

employed as potential electrode material in numerous alkaline rechargeable batteries because of its low cost, environmental compatibility, and high capacity [2–4].

Titanium dioxide (TiO_2) is broadly utilized as a coating in polymer materials because of its prominent chemical stability and low price. However, they are simple to produce electrostatic discharge and fire due to friction or collision. To avoid damage, the electrical conductivity of TiO_2 should be improved. Till now, a restricted number of investigations on the electrical properties of nanostructured TiO_2 as well as Mn_3O_4 were reported [5–7]. The low conductivity of these matters frequently requires the additive of conductive phases to increase the electron transport and the electrical contact of the active materials in the solid electrodes. Recently, titanium dioxide especially with one-dimensional TiO_2 nanotubes structures attracted significant attention as an alternative or co-material with other metal oxides in energy storage applications because it naturally provides a direct pathway for charge transfer, has a highly accessible surface, and features good electrochemical behavior and chemical stability [8–10].

The graphene exhibits many structures that make it easy to use according to different applications. Graphene oxide (GO) has both sp^2- and sp^3-hybridized carbon atoms in the hexagonal ring-based carbon networks where oxygen functional groups are created via oxidation of graphene [11–13]. Reduced graphene oxide (rGO) can be obtained from GO through reduction, that is, to eliminate the oxygen groups and fix the defects in GO to re-establish the long-range conjugated network of G and consequently restore conductivity. The rGO exhibits a considerable number of outstanding oxygen-holding functional groups on its surfaces, such as hydroxyl, carbonyl, and carboxyl groups, which can produce different types of defects [14]. These surface functional groups are useful for the collection of charges, besides they are outstanding candidates in matching with other materials or molecules such as TiO_2 and Mn_3O_4.The rGO enjoys the advantages of mechanical properties, high specific surface area, distinguished dielectric constant, and lightweight, demonstrating a definite microwave absorption function [15]. The characteristic of rGO makes them suitable candidates to be hybridized with polymer, metal oxide, and biomaterials.

Nanocomposites, which demonstrate improved mechanical and physical properties compared to their template materials, are among the most technologically hopeful materials to meet the worldwide request for high- performance applications in various fields. In that respect, the improvement of new nanocomposites with developed properties plays a significant role to expand their use in industry. As well recognized previously, the integrating of two selected TMCs into a composite provides an effective avenue to design anode materials with excellent implementation [16, 17].

Mn_3O_4 has low electrical conductivity (about 10^{-7} – 10^{-8} S/cm) [18]. Thus, scientists concentrated on synthesizing composite nanomaterials containing Mn_3O_4 to improve their efficiency as electrodes in solid batteries and supercapacitors. While high mechanical strength, thermal resistance, and respectable chemical stability of ceramics make them encouraging materials for high technology applications such as electronics, defense, aerospace, and transportation, their brittle and electrically insulating character restrict their utilization in these potential applications. Recently, graphene derivatives such as rGO have been intensively researched as conductive additives for TMO to develop their electrical conductivity to be used as electrodes in solid batteries [19–21]. This is because of the formation of a composite between a transition metal oxide with rGO, which contains oxygen groups inducing excellent hydrophilicity toward aqueous electrolyte.

We reported previously the preparation, characterization, and electrical capacitance of rGO, nanotube TiO_2, nano-Mn_3O_4, and their ternary composite [10]. In continuation of our previously published work, the present study aims to study the impact of rGO on the electrical conductivity and dielectric constant of binary and ternary composites of rGO, nanotube TiO_2, and nano-Mn_3O_4 as a function of the frequency and the temperature. The effect of frequency on the electrical properties is executed to recognize the electrical homogeneity of the matter by finding the relaxation mechanism and the class of electrical conduction through measuring the electrical parameters, viz. dc- and ac-conductivity, dielectric constant, and dielectric loss. These investigations promise to open a new era of solid-state electronics and aid us to realize the dielectric parameters of the studied materials, which are significant for material

science since they are used to determine the appropriateness for a given application [22, 23].

2 Experimental

2.1 Materials

Graphite (99.995%) was purchased from Fluke Switzerland, and hydrazine monohydrate (NH_2-$NH_2{\cdot}H_2O$)99%, potassium permanganate ($KMnO_4$) 97%, sodium nitrate ($NaNO_3$) 95%, hydrogen peroxide (H_2O_2) 30%, ethanol (C_2H_5OH) 99%, and sulfuric acid (H_2SO_4) 98% were supplied from Adwick Pharmaceutical and Chemicals Company, Egypt. Hydrochloric acid (30%), N,N-dimethylformamide (DMF), and ethylene glycol (99.8%) were provided from Merck. Commercial TiO_2 sample, ST01 was supplied from Ishihara Sangyo, Yokkaichi, Japan.

2.2 Preparation of a single material (rGO, TiO_2, and Mn_3O_4)

The methods of preparation and characterization of the individual materials (rGO, nanotube TiO_2, and Mn_3O_4) used for the formation of binary and ternary composites were reported briefly in our previous work [10]. The samples were denoted here as rGO, T, and M for reduced graphene oxide, TiO_2, and Mn_3O_4, respectively.

2.3 Preparation of binary composite

2.3.1 TiO_2@Mn_3O_4

A 2 g Mn_3O_4 and 0.7 g TiO_2 were dispersed in 100 ml de-ionized water by sonication for one hour and then introduced into 250 ml Teflon-lined autoclave and heated to 130 °C for five hours. After that, the autoclave was cooled to room temperature. The obtained precipitate was eventually washed five times with water and dried. The acquired material is denoted as T@M.

2.3.2 Preparation of Mn_3O_4@rGO

0.105 g of reduced graphene oxide (rGO) was dispersed in 100 ml de-ionized water by sonication for one hour. After that, 4 g Mn_3O_4 was added to the suspended solution with further stirring for another one hour and then transferred to a 250 ml Teflon-lined autoclave and heated to 130 °C for five hours. Finally, the autoclave was cooled to room temperature. The precipitate was then washed five times with water and dried. The obtained sample is denoted as M@rGO.

2.3.3 Preparation of TiO_2@rGO

The sample was prepared by the same mentioned method used in Sect. 2.3.2 using 0.105 g from reduced graphene oxide (rGO) and 1.4 g TiO_2 and denoted as T@rGO.

2.3.4 Preparation of Mn_3O_4@TiO_2@rGO (M@T@rGO) nanocomposite

This sample was also prepared by the same mentioned method used in Sect. 2.3.2 using 0.105 g from reduced graphene oxide (rGO), 2 g Mn_3O_4, and 0.7 g TiO_2 and denoted as M@T@rGO.

2.4 Characterization techniques

All of the synthesized samples were characterized with FT-IR spectroscopy (FT-IR spectrometer model Thermo Scientific Nicolet is10), X-ray diffraction (XRD; Model PW-3710), scanning electron microscopy (SEM) (Quanta FEG 250 worked at 20 kV), transmission electron microscope (TEM) JEOL JEM-1400), surface area and pore size analysis (Nova 2200e, Quanta chrome), and XRF fluorescence (XRF-1800, Japan) [10].

2.5 Electrical measurements

The resulting powder is pressed into pellets with a diameter of 7 mm and thickness of 1–2 mm by a brass machine under a pressure of 6 tons cm^{-2}. The electrical properties of the investigated samples were measured using a two-electrode method by the standard two-probe method. The cylindrical shape sample was painted from both sides with a silver paste and sited between two brass electrodes to guarantee a perfect composite-electrode contact. Before making the electrical measurements, the pellet samples were annealed at 200 °C for two hours. The dc-conductivity measurements were made using a Keithley 617 programmable electrometer in temperatures ranging between 30 and 300 °C. The ac measurements were performed at a constant voltage

(1 V), in a frequency ranging between 1.0×10^3 and 1×10^7 Hz, by using a programmable automatic LCR bridge (HIOKI: 3532–50).

3 Results and discussions

3.1 Characterizations

The characterizations of the tertiary M@T@rGO and its constituent materials (rGO, TiO_2, and Mn_3O_4) were reported in our published work [10]. The analysis confirmed the formation of an amorphous rGO with fiber morphological structure, nanotube anatase TiO_2, and nano-spherical particles of Hausmannite tetragonal Mn_3O_4 structures. The XRD of the binary systems investigated in the present work is given in Fig. 1. The T@ rGO spectrum shows well-established peaks credited to the (1 0 1), (0 0 4), (2 0 0), (1 0 5) (1 1 6), and (2 1 5) planes of anatase TiO_2 phase (JCPDS card No. 84- 1286). The observed broad diffraction peaks refer to the tiny particle size of TiO_2 [24]. The XRD patterns of M@RGO nanocomposite show peaks characterized for Hausmannite tetragonal Mn_3O_4 structure [JCPDS card No. 24–0734), which can be assigned to (201), (212), (103), (211), (220), (105), (321), and (400) planes. The spectrum also shows the appearance of a broad peak at ca. 23.2°, which corresponds to rGO with the interplanar spacing of 0.328 nm [25]. The XRD spectrum of the M@T binary system shows the diffraction peaks of both anatase TiO_2 and Hausmannite Mn_3O_4 phases, besides a shift of ~ 0.05° in the XRD plane (101) of bare Mn_3O_4 and ~ 0.02° of (101) and (002) plans of bare TiO_2 (inset Fig. 1). This indicates the incorporation of each metal oxide into the other.

Crystallite sizes of the investigated materials were estimated from the main diffraction peak using the Debye-Scherrer's formula given by equation [26]

$$D_{xrd} = 0.9\lambda/(\beta \cos\theta) \quad (1)$$

where D_{xrd} is the crystallite size, λ-Xray wavelength, β width at half maximum, and θ- Bragg's angle. The obtained results are listed in Table 1 and demonstrated that the particle size is dependent on the sample composition and has values of 17.0, 31.4, and 28.7 nm for T@rGO, M@rGO, and M@T, respectively.

The FT-IR spectra of the investigated samples are shown in Supplementary Fig S1a-j where the FT-IR spectra of the individual constituents of the oxides

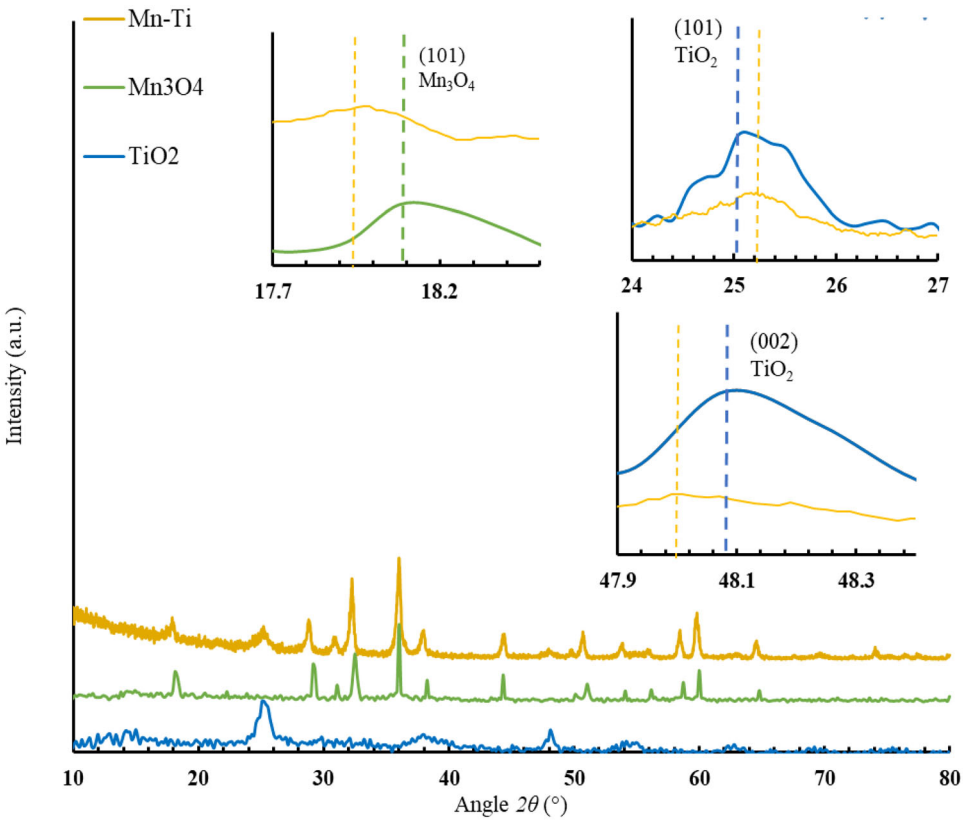

Fig. 1 XRD of the investigated materials

Table 1 Particle size and BET data of the as-prepared materials

Sample	Particle Size (nm)	Surface area (m^2/g)	Pore diameter (nm)
rGO*	–	309.9	8.2
M@Rgo	31.4	208.3	12.5
M@T	28.7	98.2	9.3
T@rGO	17.0	130.3	8.7
T*	12.9	28.6	10.0
M@T@rGO*	35.0	55.8	15.5
Mn_3O_4*	58.9	14.4	7.8

*Data reported in our previous work [10]

and their binary and ternary nanocomposites are compared. For rGO, the peaks observed at 3420, 1735, 1623, 1375, 1227, and 1023 cm^{-1} correspond to the C–OH, C = O, aromatic C = C, C–OH, C–O–C, and alkoxy C-O stretching vibrations, respectively. [27]. The FT-IR spectrum of Mn_3O_4 illustrates vibration frequencies at 627 and 491 cm^{-1} corresponding to Mn–O stretching modes in tetrahedral and octahedral sites, respectively, besides broadband at 3425 and another weak band at 1622 cm^{-1} due to absorbed water [28], whereas in the FT-IR spectrum of TiO_2 peaks are observed at 453 cm^{-1} and 732 cm^{-1} corresponding for O–Ti–O bonding in anatase morphology [29]. For composite samples, the FT-IR spectra show some characters revealing the interactions occurring between all the constituents. The spectrum of M@rGO shows almost the disappearance of C-O absorption of rGO bands besides a reduction in the intensity of absorption peaks of O–H. This suggests the formation of weak interaction in Mn–O-C [30]. Furthermore, the intensities of the tetrahedral and octahedral bands present in the spectrum of Mn_3O_4 in the range of 450–650 are slightly shifted referring to effective interaction between the portions creating the composite. The spectrum of M@rGO also shows that the band area ratio of tetrahedral/octahedral in the binary system is greater than that in the pure Mn_3O_4 sample. The FT-IR spectrum of T@rGO shows a wide absorption band centered at 3370 cm^{-1} due to the residual O–H groups of rGO. Thus, TiO_2 has a chance to interact with these functional groups during the formation of the nanocomposites [31]. The FT-IR spectrum of M@T shows a shift in the main characteristic bands of the individual constituents at1585, 1150, 590, and 475 cm^{-1}.

The surface and pore-size distribution were carried out for the investigated materials and the obtained results show hysteresis loops, as illustrated in Supplementary Fig. S2. The analyses of the data are summarized in Table 1, with those reported in our previous work [10]. The obtained data show that the specific surface area of the investigated materials ranks in the order:

$$rGO > M@rGO > M@T > T@rGO > M@T@rGO > T > Mn_3O_4$$

whereas the pore-size diameter shows a mesoporous structure increasing according to the following order:

$$M@T@rGO > M@rGO > T > M@T > T@rGO > rGO > Mn_3o_4$$

The SEM and TEM micrographs of the synthesized composites and their components are displayed in Figs. 2 and 3, respectively. The SEM and TEM images of the rGO sample (Figs. 2a and 3a) show fiber structure with diameters of 10 nm for rGO. The SEM and TEM micrographs of TiO_2 (Figs. 2b and 3b) show nanotubes with an average diameter and length of 5 and 150 nm, respectively. The photographs of Mn_3O_4 (Figs. 2c and 3c) show a mixed morphology with the majority of deformed spheres. The images of the ternary system MTrGO (Figs. 2d and 3d) show mixed nanoparticles of the constituent materials accompanied by a considerable decrease in the fiber lengths. The SEM and TEM photographs of $M@rGO_4$ (Figs. 2e and 3e) show deformed spherical particles covered with rGO fibers, whereas the images of T@rGO (Figs. 2f and 3f) illustrate nanotube structures of TiO_2 decorated with rGO fibers. This refers that the rGO covered the investigated metal oxides without changing their morphological structure. Moreover, the images suggest the presence of an association between the rGO and metal oxide nanoparticles. The SEM and TEM images of binary mixed metal oxide sample M@T (Fig. 2g and 3g) show the interference

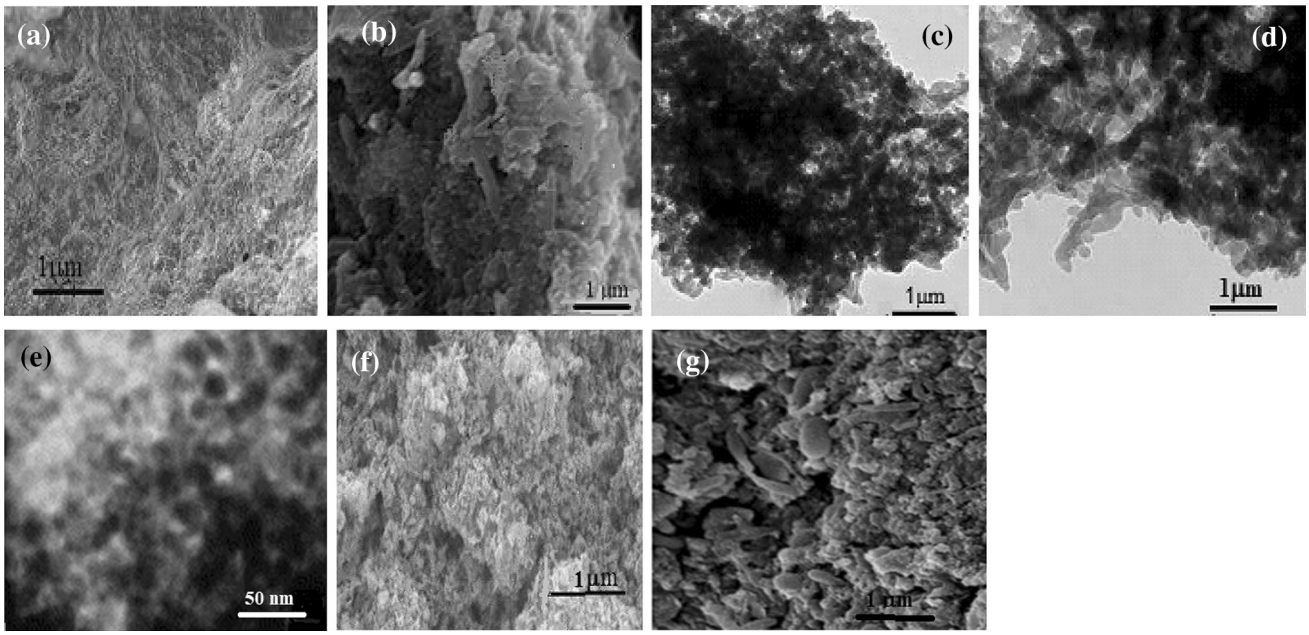

Fig. 2 SEM of **a** rGO, **b** T, **c** M, **d** M@T@rGO, [published in our previous work [10]] as well as **e** M@rGO, **f** T@rGO, and **g** M@T samples

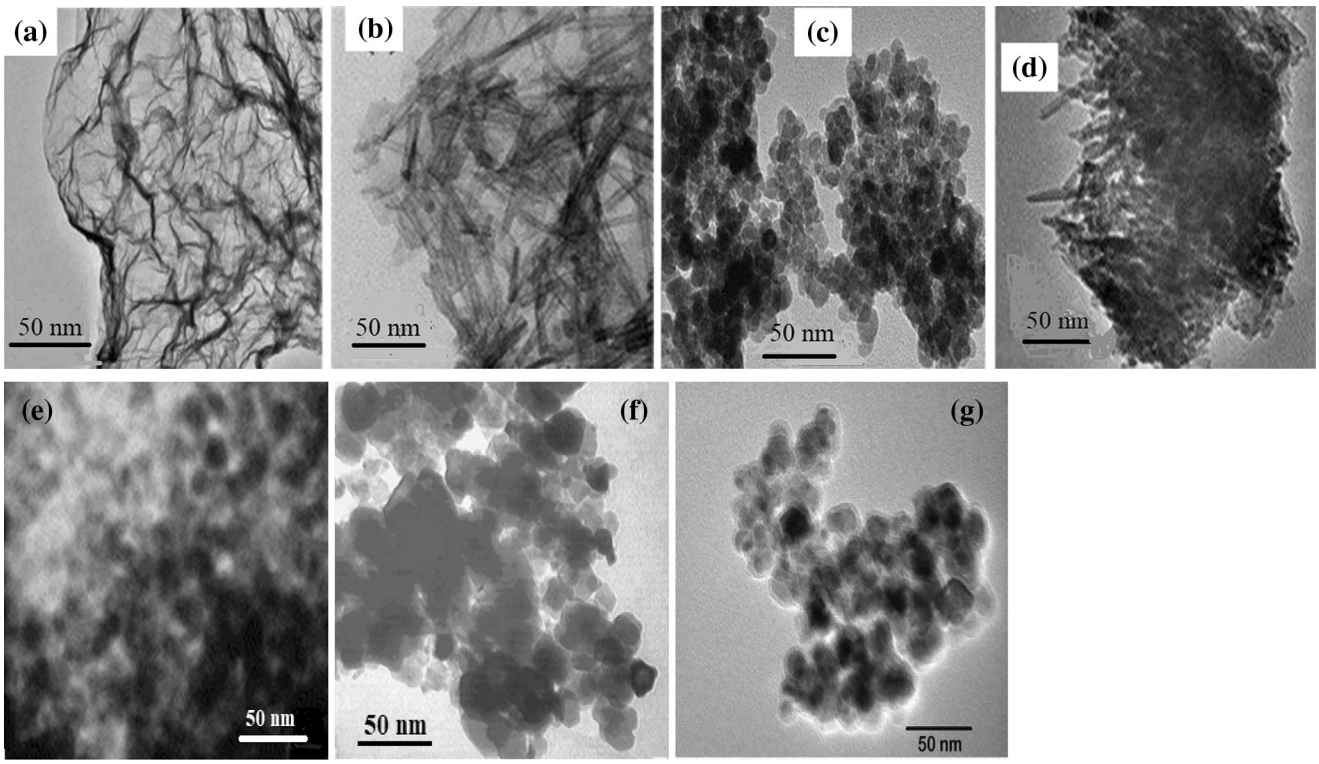

Fig. 3 TEM of **a** rGO, **b** T, **c** M, **d** M@T@rGO, [published in our previous work [10]] as well as **e** M@rGO, **f** T@rGO, and **g** M@T samples

of the nanotubes of TiO_2 with the spherical particles of Mn_3O_4 constituent. From the obtained micrographs, it can be also seen that in the presence of rGO suspension, TiO_2 and Mn_3O_4 grow to smaller particles than their sizes, besides they are dispersed on the surface of rGO. It is attributed to the fact that the

abundant oxygen-encompassing groups of rGO absorb and/or fix metal oxide particles and limit them to develop bigger and agglomerate. The oxygen-holding functional groups, such as hydroxyl and epoxy groups, play an actual significant role in the anchoring of metal oxide nanoparticles on the surface of rGO. The covered metal oxide particles with rGO are also approved by their higher specific surface areas, as listed in Table 1.

The high-resolution TEM of the binary investigated system, in the present work, is done and the images obtained are shown in Fig. 4a–c. The crystal lattice fringe of Mn_3O_4 in M@rGO (Fig. 4 a) shows a d-spacing of 0.25 nm corresponding to the (211) plane [32]. The crystal lattice fringe of TiO_2 in T@rGO has a d-spacing of 0.355 nm corresponding to the (101) plane [33], whereas, the crystal lattice fringes of TiO_2 and Mn_3O_4 in the M@T sample exhibit values of 0.238 and 0.352 nm for (211) and (101) planes, respectively, which are less than that found in each of M@rGO and T@rGO. This could be attributed to the different types of interactions occurring between the particles present in the samples.

The XRF analyses showed results inconsistent with the constitution of the initial feeding ratios of starting materials.

3.2 Electrical properties

3.2.1 DC-measurements

The conductivity is considered as the conducting power inside the material. Therefore, the dc-electrical conductivity of the investigated samples was studied in temperatures ranging between 30 and 300 °C. The obtained results are shown in Fig. 5 in the form of ln (σ_{dc}) versus $10^3/T$. It shows that the conductivity increases with temperature in a manner that follows approximately the Arrhenius trend behavior with activation energy, E_a, depending on the composition of the sample. The conductivity data are summarized in Table 2. The electrical conductivity of TiO_2 is related to the thermal ionization of Ti^{3+} ions (Ti^{3+} / Ti^{4+}) with the delocalization of the electrons [34], whereas the electrical conductivity of Mn_3O_4 is attributed to the thermally activated polaronic hopping of electrons from Mn^{2+} ions in the octahedral site to Mn^{3+} ions in the tetrahedral sites.[35]. The high electrical conductivity of T@M than that of Mn_3O_4 can be explained on the basis that the Ti^{4+} act as donors by supplying free electrons when occupying (Mn^{2+} or Mn^{3+}) ion sites in Mn_3O_4. Table 2 also shows that the conductivity values of the nanocomposites containing rGO are significantly greater than those obtained for the pure Mn_3O_4 and TiO_2. This can be explained based on the generation of new electron energy levels and conduction channels of a three-dimensional conductive network formed by bridging rGO with the other metal oxide. This tactic can offer a new attitude to improve the conductivity of TiO_2-based conductive materials and simplify its use in the coating field to eliminate the electrostatic discharge and fire due to friction or collision of pure TiO_2 with low conductivity. The obtained activation energies of pure materials agree well with that reported for Mn_3O_4 (0.75 eV) [35] and (0.87 eV) for nanotube TiO_2 [36].

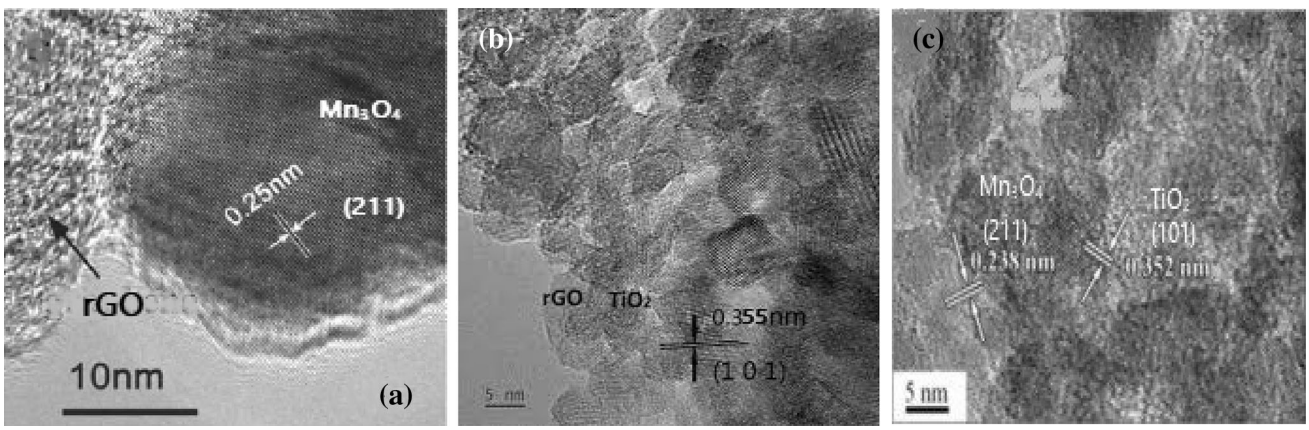

Fig. 4 HRTEM of **a** M@rGO, **b** T@rGO, and **c** M@T materials

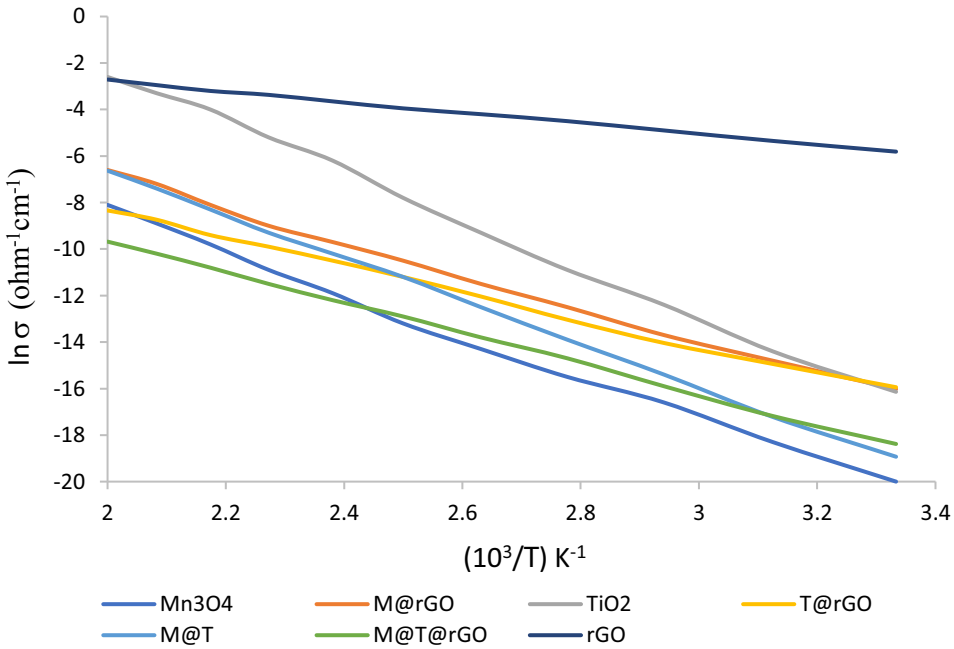

Fig. 5 Effect of temperature on the dc-electrical conductivity of the investigated materials

Table 2 DC-conductivity data of the investigated samples

Sample	σ_{300} (ohm^{-1} cm^{-1})*	Activation energy (eV)
rGO	2.99×10^{-3}	0.20
TiO_2 (T)	9.88×10^{-8}	0.86
Mn_3O_4 (M)	2.06×10^{-9}	0.79
T@rGO	1.19×10^{-7}	0.49
M@rGO	1.11×10^{-7}	0.61
M@T	6.01×10^{-9}	0.75
M@T@rGO	1.04×10^{-8}	0.56

*σ_{300} specific electrical conductivity at 300 K

3.2.2 *AC measurements*

3.2.2.1 AC-conductivity analysis The effect of frequency on ac-conduction is done to know the electrical homogeneity of the material by characterizing the electrical conductivity, electric permittivity, and energy loss, which are significant parameters for material science because these parameters are used to determine the suitability for a given application [22, 23].

The frequency dependence of ac-conductivity (σ_{ac}) for all the studied materials, at room temperature, is shown in Fig. 6. The ac-electrical conductivity (σ_{ac}) is calculated according to the following equation:

$$\sigma_{ac} = \omega \varepsilon_o \varepsilon' \tan \delta \quad (2)$$

where ω is the angular frequency, ε_o is the constant of the permittivity of free space, ε' is the relative permittivity, and tan δ is the loss factor. Figure 5 shows that the electrical conductivity (σ_{ac}) for all samples raises with the increase in applied frequency. This is attributed to the pumping force of the applied frequency of ac-field aids in moving the electronic charges between the different localized states and releasing trapped charges from the various trapping centers. These charge carriers share in the conduction course at the same time as the electrons generated from the valence switching between the diverse metal ions present in the sample [37].

It is well known that the ac-conductivity of highly disordered materials with amorphous semiconductors as well as ionic conducting materials obeys the following equation [38]:

$$\sigma_{ac}(\omega) = B\omega^s \quad (3)$$

where B and s both are constants depending on each of the temperature and composition. The experimental values of s obtained for all compositions are obtained from the slopes of the plots of log σ_{ac} *vs.* log w and found to be 0.57, 0.51, 0.53, 0.46, 0.53, 0.52, and 0.02 for M, M@rGO, T, T@rGO, M@T, M@T@rGO, and rGO, respectively. These values agree well (except for rGO) with the values (0.6–1.0) found for the hoping mechanism in the most transition metal oxide materials [39]. The high σ_{ac} – values observed at the

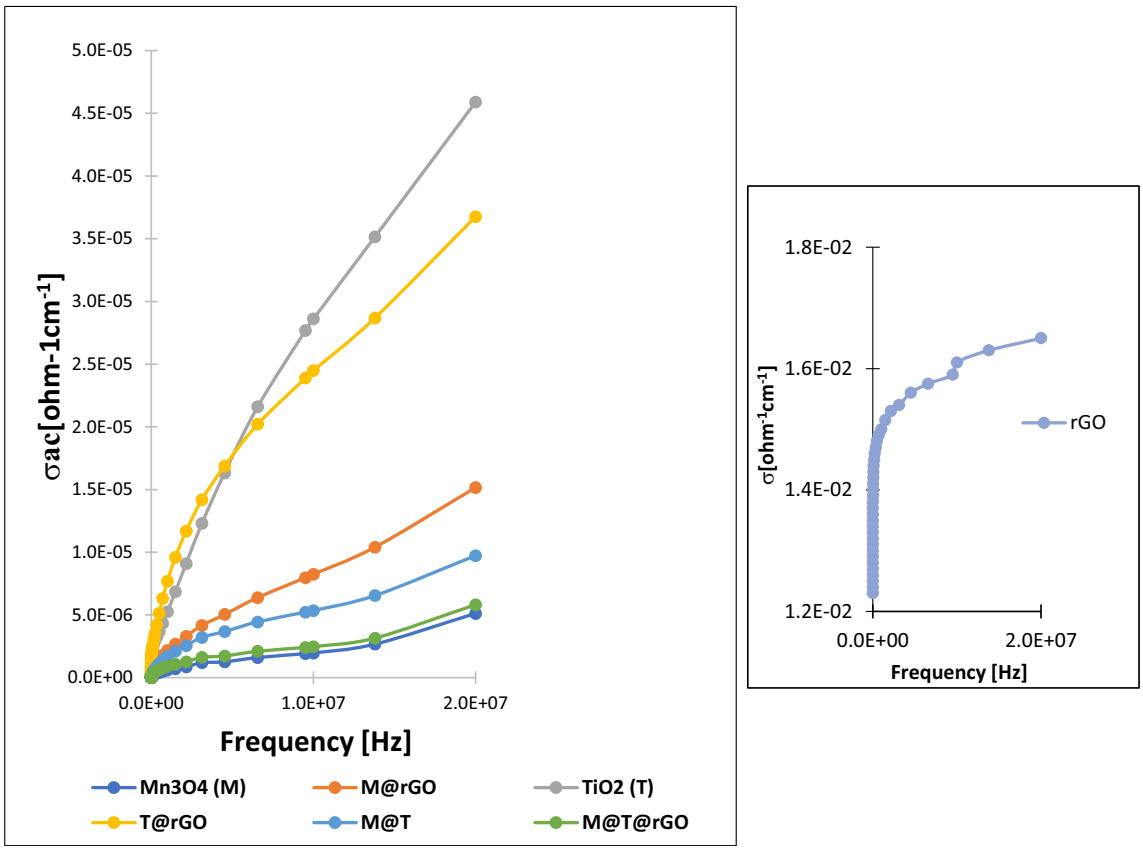

Fig. 6 Effect of frequency on ac-electrical conductivity of the investigated materials

high frequencies is also a characteristic trend involved for a small polaron hopping mechanism. In the nanomaterial systems, the conductivity displays with high-localized carriers bind to the lattice with a lattice strain i.e., with polaron conduction. The obtained results, illustrated in Fig. 7, shows that the ac-conductivity value is enhanced by the blending of the rGO with the metal oxides and follows the order:

$$\text{rGO} > \text{T@rGO} > \text{TiO}_2 > \text{M@rGO} > \text{M@T} > \text{M@T@rGO} > \text{Mn}_3\text{O}_4$$

The conductivity value obtained for the TiO_2-rGO composite showed the highest one in all the investigated composite samples. Thus, we expect that this T@rGO composite sample exhibits the best one of the investigated materials for application in the photocatalytic process.

3.2.3 *Dielectric analysis*

The complex dielectric constant (ε^*) of a dielectric material placed in the ac electric field describes the most important electrical property of the materials and depends on the strength of electromagnetic interactions between component phases, the relative majority of one phase over the other, and the microstructure of phases [40]. ε^* is signified by $\varepsilon^* = \varepsilon' - i\varepsilon''$ where ε' is the real dielectric constant which characterizes the energy stored in the dielectric material and ε'' is the imaginary part of the dielectric complex representing the energy losses by a dielectric material and the ratio ($\varepsilon''/\varepsilon'$) represents the loss tangent factor *tan* δ. The dielectric measurements were operated in the lower frequency range of 10^3–10^7 Hz for demonstrating the relative assessment of their response to electromagnetic (EM) waves.

The dielectric constant ε' and the dielectric loss ε'' were determined by the following relations: $\varepsilon/=Cd/A\varepsilon o$ and

$$\tan\delta = \varepsilon'/\varepsilon'' \quad (4)$$

where C is the capacitance of the pellet, d the thickness of the pellet, and A the cross-sectional area of the flat surface of the pellet.

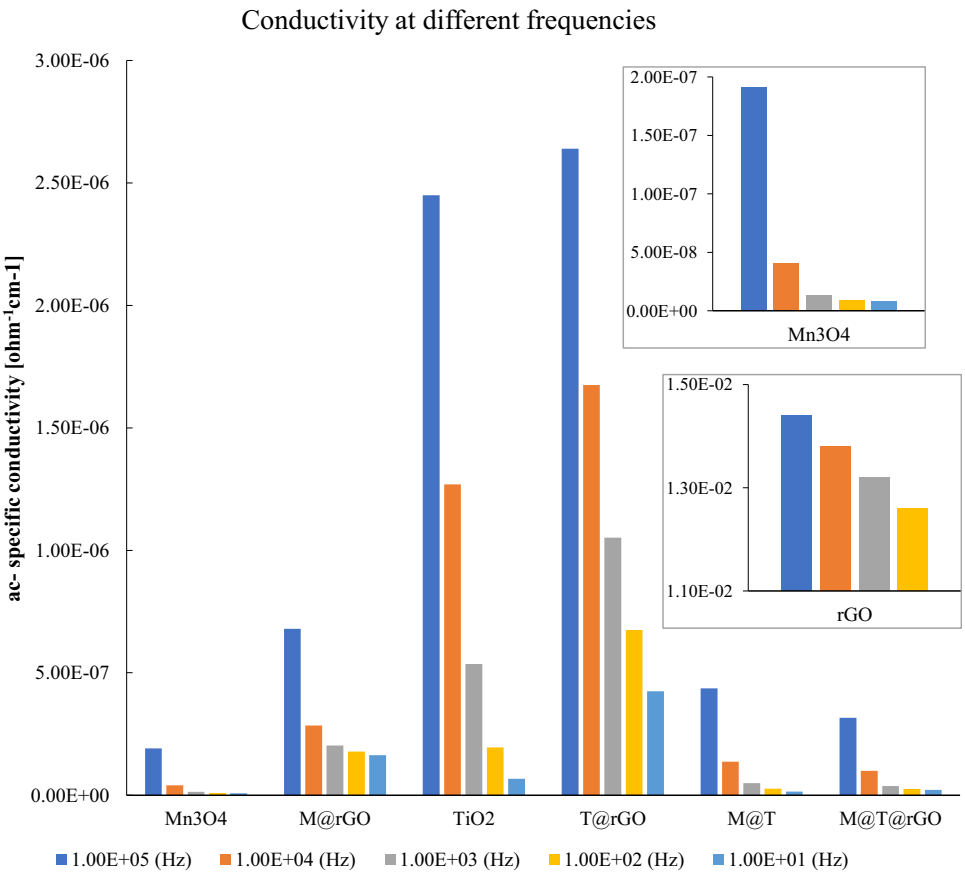

Fig. 7 σ_{ac}- of the investigated materials at several frequencies at room temperature

The effect of frequency on the real dielectric constant (ε′), for all investigated materials, can be seen from Fig. 8, which shows that the ε′ value lessens continuously with increasing frequency and reaches a constant value at higher frequencies. This can be explained on the basis that at low frequency the electrical dipoles can track the frequency of the applied electric field, whereas at high frequency the dipoles are unable to track the frequency of the applied field.

For Mn_3O_4, the frequency dependence of the dielectric constant can be interpreted based on Koops [41] theory and the Maxwell–Wagner [42–44] theory. As suggested by these theories, a dielectric material is comprised of two layers: conductive grains isolated by conductive grain boundaries which are poorly resistive. At lower frequency, the large value of ε/ is caused by low conduction, while at a higher frequency the manganite grains of moderate conductivity are prominent.

It can be also said that at lower frequencies, the polarization development in Mn_3O_4 nanoparticles can be clarified based on a neighboring movement of electrons by hopping mechanism between the various oxidation states of Mn-ion and alignment of the electric dipole in the track of the applied field. With rising frequency, a reduction occurs in each of the electric dipoles, the Mn^{2+}/Mn^{3+} electron transfer, the net shift of charge in one direction, and thus the $\varepsilon^{/}$-values decreases. The high dielectric constant values of Mn_3O_4 can be also explained on the basis that Mn_3O_4 nanoparticles contain a huge number of particles per unit volume causing the intensification of the dipole moment per unit volume and the formation of the high dielectric constant.

For the TiO_2 sample, the high ε′ value observed for TiO_2 denotes that the polarization mechanism in the TiO_2 nanocrystals is predominantly attributed to the space charge polarization due to the accumulation of the charges at the grain boundary of TiO_2 nanotubes.

The rGO has dangling bonds and residual oxygen-encompassing functional groups on its surface, such as hydroxyl, carboxyl, carbonyl, and epoxy groups, which can produce defects such as defect polarization and electron dipole relaxation [14]. These defects besides the high conductivity and the large numbers

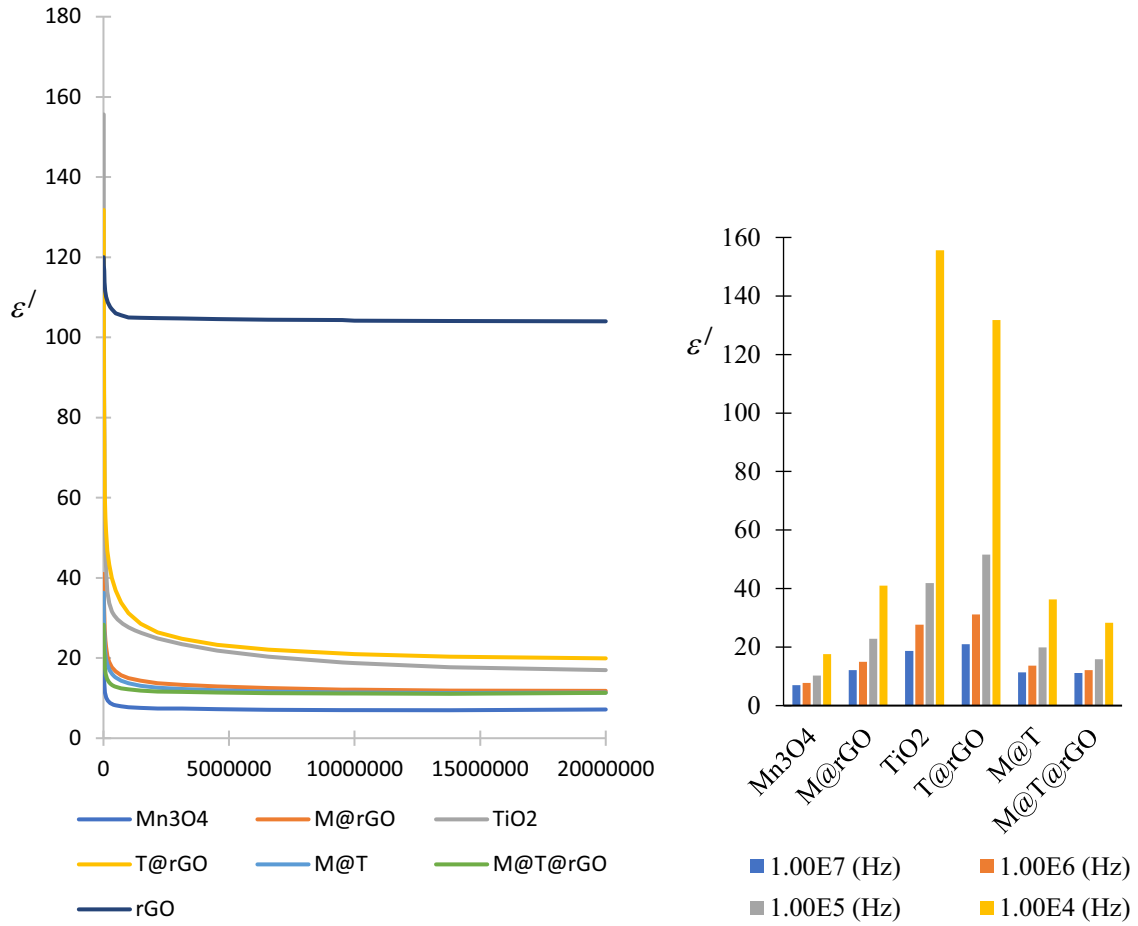

Fig. 8 Effect of frequency on the dielectric constant of the investigated materials

of interfaces ensure rGO with excellent dielectric property (relative permittivity of 915 at 50 Hz), marking a phenomenon referred to as colossal dielectricity. The rGO has a big specific surface area, high dielectric constant, and lightweight, which manage it as an appealing candidate for microwave absorber [15]. However, the overall attenuation effect of a single rGO on electromagnetic waves is still relatively weak. Mn_3O_4, as a dual-composite material, can produce both magnetic loss and dielectric loss, so it has respectable electromagnetic properties and cab improve microwave absorption.

The dielectric constant (ε′) for M@T nanocomposite has a high value in the low- frequency region. This is attributed to the presence of several types of polarization mechanisms like electronic, ionic, orientation, and space charge polarization, and the surface charge polarization is ruminated to be more prominent [45]. At low frequencies, the polarization process is elucidated as a local displacement of electrons by a hopping mechanism between Mn^{2+} and Mn^{3+} and the orientation of electric dipoles in the direction of the applied field. With raising the frequency, electron transport between the charged states and the net displacement of charge in one direction decreases, and then the dielectric constant reduces. Therefore, the dielectric constant becomes very low and keeps constant at higher frequencies as shown in Fig. 8.

In general, the results (represented in Fig. 8) show that at a fixed frequency, the dielectric constant increases in the order:

$$TiO_2 > T@rGO > M@rGO > M@T > M@T@rGO > Mn_3O_4 > rGO$$

This order differs from that observed for the ac-electrical conductivity. This means that the contribution of polarization in the conductivity values depends on the composition of the sample which predominates polarization depends to a large extent on the individual constituent in the sample and its

morphological structure as well as the type and the number of defects present in it.

The frequency dependence of the dielectric loss (ε″) of the investigated Materials, represented in Fig. 9, shows the same trend of dielectric constant. The ε″-value increases in the order:

$$T@rGO > TiO_2 > rGO > M@rGO > M@T > M@T@rGO > Mn_3O_4$$

The obtained results also showed that the ε″ value depends on the composition of the sample. The observed outstanding ε″ values of the nanocomposites at lower frequencies come from the Debye dipolar polarization relaxation, interfacial polarization relaxation, and the exceptional conductivity of rGO, etc. [46, 47]. In metal oxides, the dipole polarization and electrons are not consistent with the variations of the electromagnetic field in the high frequency which is conducted to the Debye relaxation backing to the dielectric loss. In the composite materials, the vacancies at the interfaces between the metal oxides nanoparticles and the rGO [46, 48], in cooperation with the defects on the graphene fibers produced by the bad extreme restacking of the fibers could proceed as polarized centers for the dipole polarization relaxation, improving the dielectric loss and electromagnetic energy dissipation [49]. Moreover, the high conductivity of the rGO causes the formation of some conductive micro-networks in the nanocomposites containing rGO. This leads to a decrease in resistivity and makes a polarization in the internal medium and in turn increases the dielectric loss due to fluctuation of the electronic field and transforms the electromagnetic energy into thermal energy [50]. The high $\varepsilon^{//}$ value observed in M@rGO could be also related to the electron hopping between the different valency states of manganese ions, such as Mn^{2+} and Mn^{3}, through the conductivity tracks built by the rGO due to the application of the electromagnetic wave.

3.2.4 *Electrochemical impedance spectroscopy (EIS) measurements*

EIS is a valuable method to illustrate the charge carrier movement. EIS study was performed at room temperature for the examined materials to give more information on grain, grain boundary, electrode interfaces, and the charge transport presentation of the investigated materials. The data obtained are illustrated as Cole–Cole diagrams (Z″ vs. Z′) in Fig. 10. A small portion of the impedance dispersion profile can be only noticed due to the very high

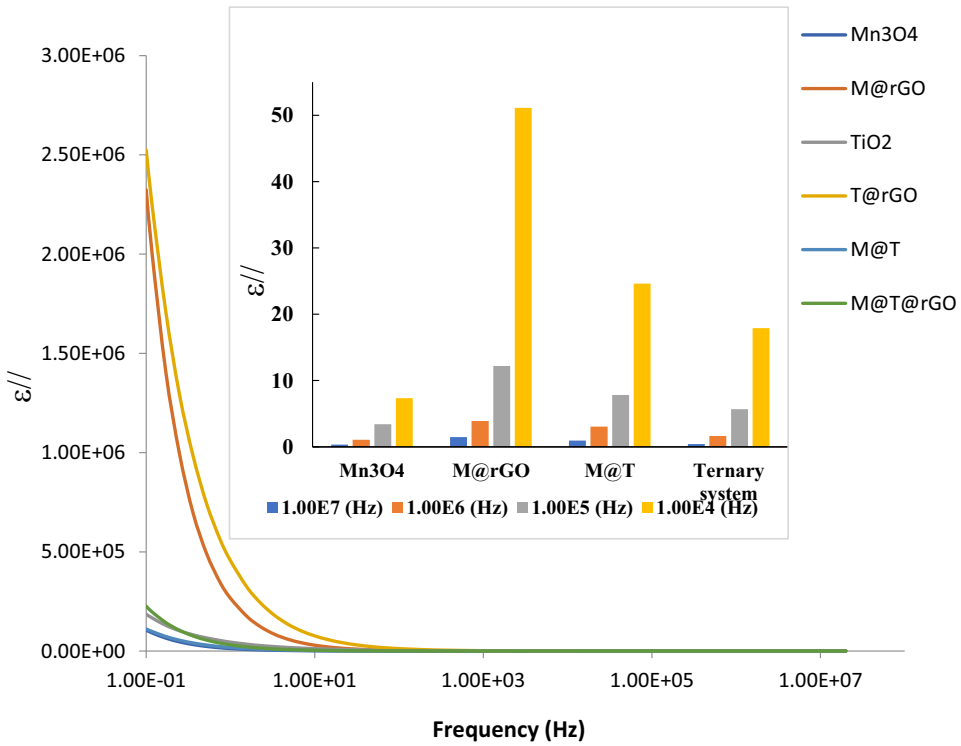

Fig. 9 Effect of frequency on the dielectric loss of the investigated materials

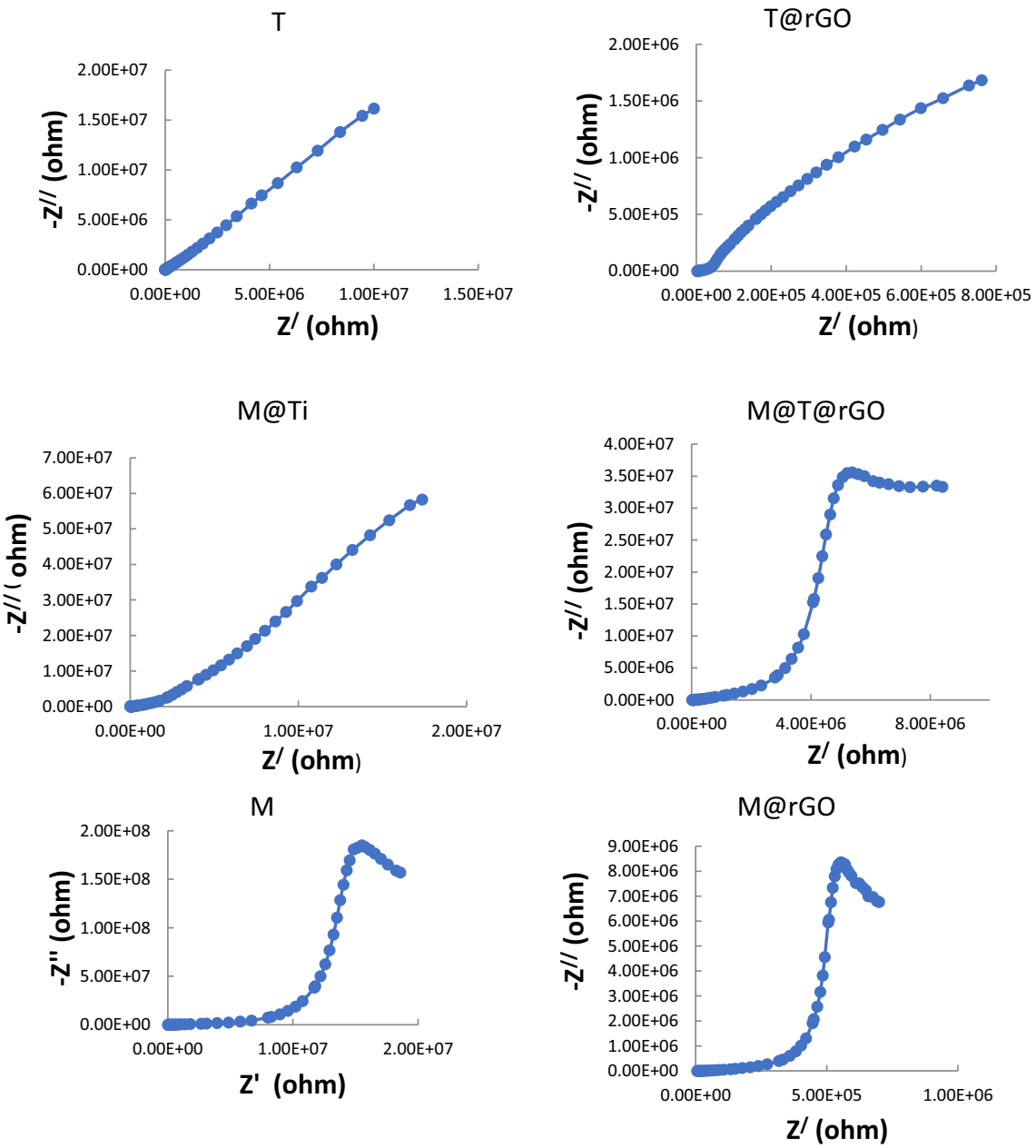

Fig.10 Cole–Cole diagrams of the investigated materials

resistivities of the investigated samples arising mainly from the grain boundary. Generally, the EIS measurements can also distinguish between the different influences of the grain boundary and the grain bulk of the material when there is satisfactorily considerable differentiation in the time constants [51]. The Cole plots of TiO_2 and M@T samples did not show semicircle as a result of the grain bulk. This may be attributed to that relaxation time ($\tau = RC$) in the grain bulk regions lies at a frequency higher than the range of measurements (10 MHz) [52], whereas, for the samples containing rGO, the only grain boundary response almost start to appear at the lower frequencies, while the more conductive bulk is not observed at the higher frequencies of the plots. This could be attributed to that the conductive rGO fibers could serve as a fast electron transport path in the material. The presence of rGO in the composite system facile the transfer of electrons from the CB of metal oxide into rGO, while the positive hole confined in metal oxide will have a longer lifetime to disperse to the surface [53]. The Cole diagrams of all

the investigated samples did not also show spikes at the low-frequency range. This refers to that the electrons are the conducting species in all the investigated materials.

4 Conclusions

Electrical properties of binary and ternary nanocomposites formed from nano-Mn_3O_4 nanoparticles, nanotubes TiO_2, and rGO were studied. The electrical conductivity of all the investigated materials, except rGO, follow the semiconducting behavior. The conductivity increased with introducing rGO into the metal oxides due to the formation of a bridge between the metal ions and followed the order: rGO > T@rGO > T > M@rGO > M@T > M@T@rGO > M. The high conductivity value of T@rGO refers to the possibility of using it as a coating material and for the application in the photocatalytic process. The dielectric constant (ε') and dielectric losses (ε'') values of all materials showed a monotonous decrease with an exponential behavior by increasing the applied ac-frequency. At constant frequency, the ε' value followed the order: T > rGO > T@rGO > M@rGO > M@T > M@T@rGO > M, whereas the ε'' value followed the order: T@rGO > Ti > rGO > M@rGO > M@T > M@T@rGO > M. The dielectric properties explained on the basis of Maxwell Wagner model. The electrons are the conducting species in all the investigated materials. Moreover, the introduction of the metal oxides into the rGO matrix affects their electrical properties owing to the combined effect of the redox reaction of metal oxides and the large surface area and the electrical conductivity of rGO.

Funding

No Funding was recieved.

Supplementary Information: The online version contains supplementary material available at https://doi.org/10.1007/s10854-021-05678-z.

References

1. M. Liu, Y. Wang, Z. Cheng, M. Zhang, M. Hu, J. Li, Electrospun Mn_2O_3 nanowrinkles and Mn_3O_4 nanorods: morphology and catalytic application. Appl. Surf. Sci. **313**, 360–367 (2014)
2. X. Li, P.F. Liu, L. Zhang, M.Y. Zu, Y.X. Yang, H.G. Yang, Enhancing alkaline hydrogen evolution reaction activity through Ni–Mn_3O_4 nanocomposites. Chem. Commun. **52**, 10566 (2016)
3. M. Fang, X. Tan, M. Liu, S. Kang, X. Hu, L. Zhang, Low-temperature synthesis of Mn_3O_4 hollow-tetrakaidecahedrons and their application in electrochemical capacitors. Cryst. Eng. Comm. **13**, 4915–4920 (2011)
4. A. Vázquez-Olmos, R. Redón, G. Rodríguez-Gattorno, M.E. Mata-Zamora, F. Morales-Leal, A.L. Fernández-Osorio, J.M. Saniger, One-step synthesis of Mn_3O_4 nanoparticles: Structural and magnetic study. J. Colloid Interf. Sci. **291**(1), 175–180 (2005)
5. D. Yan, S. Cheng, R.F. Zhuo, J.T. Chen, J.J. Feng, H.T. Feng, H.J. Li, Z.G. Wu, J. Wang, P.X. Yan, Nanoparticles and 3D sponge-like porous networks of manganese oxides and their microwave absorption properties. J. Nano. Technol. **20**(10), 105706 (2009)
6. G. Kaur, P. Negi, M. Kaur, R. Sharma, R.J. Konwar, A. Mahajan, Morpho-structural and opto-electrical properties of chemically tuned nanostructured TiO_2. Ceram. Intern. **44**(15), 18484–18490 (2018)
7. E. Karaoğlu, H. Deligöz, H. Sözeri, A. Baykal, M.S. Toprak, Hydrothermal synthesis and characterization of PEG-Mn_3O_4 nanocomposite. J. Nano-Micro Lett. **3**, 25–33 (2011). https://doi.org/10.3786/nml.v3i1
8. Y. Xie, L. Zhou, C. Huang, H. Huang, J. Lu, Fabrication of nickel oxide-embedded titania nanotube array for redox capacitance application. Electrochim. Acta. **53**(10), 3643–3649 (2008)
9. H.T. Fang, M. Liu, D.W. Wang, T. Sun, D.S. Guan, F. Li, J. Zhou, T.K. Sham, H.M. Cheng, Comparison of the rate capability of nanostructured amorphous and anatase TiO_2 for lithium insertion using anodic TiO_2 nanotube arrays. J. Nano technol. **20**(22), 225701–225707 (2009)
10. M. El-Shahat, M. Mochtar, M.M. Rashad, M.A. Mousa, Single and ternary nano composite electrodes of Mn_3O_4/TiO_2/rGO for supercapacitors. J. Solid Stat. Elect. (2021). https://doi.org/10.1007/s10008-020-04837-2
11. K.S. Novoselov, A.K. Geim, S.V. Morozov, D. Jiang, M.I. Katsnelson, I.V. Grigorieva, S.V. Dubonos, A.A. Firsov, Two-dimensional gas of massless dirac fermions in graphene. J. Nature. **438**, 197–200 (2005)

12. Y.B. Zhang, Y.W. Tan, H.L. Stormer, P. Kim, Experimental observation of the quantum hall effect and Berry's phase in graphene. J. Nature. **438**, 201–204 (2005)
13. J.C. Meyer, A.K. Geim, M.I. Katsnelson, K.S. Novoselov, T.J. Booth, S. Roth, The structure of suspended graphene sheet. J. Nature. **446**, 60–63 (2007)
14. H.G. Yu, C.L. Chu, P.K. Chu, Self-assembly and enhanced visible-light-driven photocatalytic activity of reduced graphene oxide-Bi_2WO_6 photocatalysts. J. Nano. Technol. Rev. **6**(6), 505–516 (2017)
15. Z. Jiao et al., Carboxymethyl cellulose-grafted graphene oxide for efficient antitumor drug delivery. Nano. Technol. Rev. **7**(4), 291–301 (2018)
16. Y. Luo, D. Kong, J. Luo, Y. Wang, D. Zhang, K. Qiu, C. Cheng, C.M. Li, T. Yu, Seed assisted synthesis of Co_3O_4@α-Fe_2O_3 core–shell nanoneedle arrays for lithium-ion battery anode with high capacity. RSC Adv. **4**, 13241–13249 (2014)
17. L. Hou, L. Lian, L. Zhang, G. Pang, C. Yuan, X. Zhang, Self-sacrifice template fabrication of hierarchical mesoporous bi-component-active ZnO/$ZnFe_2O_4$ sub-microcubes as superior anode towards high-performance lithium-ion battery. Adv. Funct. Mater. **25**(2), 238–246 (2015)
18. J. Zhu, R. Duan, S. Zhang, N. Jiang, Y. Zhang, J. Zhu, The application of graphene in lithium ion battery electrode materials. SpringerPlus. **3**, 585 (2014)
19. H. Yin, C. Zhang, F. Liu, Y. Hou, Hybrid of iron nitride and nitrogen- doped graphene aerogel as synergistic catalyst for oxygen reduction reaction. J. Adv. Funct. Mater. **24**(20), 2930 (2014). https://doi.org/10.1002/adfm.201303902
20. A. Jana, E. Scheer, S. Polarz, Synthesis of graphene–transition metal oxide hybrid nanoparticles and their application in various fields. Beilstein J. Nanotechnol. **8**, 688–714 (2017)
21. T. Liu, S. Sun, Z. Zang, X. Li, X. Sun, F. Caoa, J. Wu, Effects of graphene with different sizes as conductive additives on the electrochemical performance of a $LiFePO_4$ cathode. J. RSC Adv. **7**, 20882–20887 (2017)
22. L. Solymar, D. Walsh, R. R. A. Syms, Electrical properties of materials, Ninth Edition, (Oxford university press, 2014).
23. M. E. Achour, R. Touahni, R. Messoussi, M. Elaatmani, M.A. Ali, Dielectric Materials and Applications. Mater. Res. Proceed. **1**, (2016)
24. R.K. Nainani, P. Thakur, Facile synthesis of TiO_2-RGO composite with enhanced performance for the photocatalytic mineralization of organic pollutants. J. Water Sci Technol. **73**(8), 1927–1936 (2016)
25. J.W. Lee, A.S. Hall, J.D. Kim, T.E. Mallouk, A facile and template-free hydrothermal synthesis of Mn_3O_4 nanorods on graphene sheets for supercapacitor electrodes with long cycle stability. J. Chem. Mater. **24**, 1158–1164 (2012)
26. A.L. Patterson, The scherrer formula for x-ray particle size determination. Phys Rev. **56**, 978–982 (1939)
27. D. Kong, L.T. Le, Y. Li, J.L. Zunino, W. Lee, Temperature-dependent electrical properties of graphene inkjet-printed on flexible materials. Langmuir **28**(37), 13467–13472 (2012)
28. J.M. Boyero et al., Influence of the synthesis parameters on the structural and textural properties of precipitated manganese oxides. Int. J. Inorg. Mater. **3**(7), 889–899 (2001)
29. G.J. de, A.A. Soler-Illia, A. Louis, C. Sanchez, Synthesis and characterization of mesostructured titania-based materials through evaporation-induced self assembly. Chem. of Mater. **14**(2), 750–759 (2002)
30. D. Joung, V. Singh, S. Park, A. Schulte, S. SeaL, S.I. Khondaker, Anchoring ceria nanoparticles on reduced graphene oxide and their electronic transport properties. J. Phys. Chem. C. **115**(50), 24494–24500 (2011)
31. M.S.S. Shah, A.R. Park, K. Zhang, J.H. Park, P.J. Yoo, Green synthesis of biphasic TiO_2-reduced graphene oxide nanocomposites with highly enhanced photocatalytic activity. ACS Appl. Mater. Interf. **8**(8), 3893–3901 (2012)
32. J. Wang, H. Zhao, J. Song, T. Zhu, W. Xu, Structure-Activity relationship of manganese oxide catalysts for the catalytic oxidation of (chloro)-VOCs. Catalysts. **9**, 26 (2019). https://doi.org/10.3390/catal9090726
33. B.V. Dimas et al., Atomic-Scale investigation on the evolution of TiO_2 anatase prepared by a sonochemical route and treated with NaOH. Materials (Basel). **13**, 685 (2020). https://doi.org/10.3390/ma13030685
34. R.B. Belgacem, M. Chaari, A. Matoussi, Studies on structural and electrical properties of ZnO/TiO_2 composite materials. J. Alloys Compd. **651**, 49–58 (2015)
35. V.C. Bose, K. Maniammal, G. Madhu, C.L. Veenas, A.S.A. Raj, V. Biju, Electrical conductivity of nanocrystalline Mn_3O_4 synthesized through a novel sol-gel route. Mater. Sci. and Eng. **73**, 012084 (2015). https://doi.org/10.1088/1757-899X/73/1/012084
36. R. Asmatulu, A. Karthikeyan, D.C. Bell, S. Ramanathan, M.J. Aziz, Synthesis and variable temperature electrical conductivity studies of highly ordered TiO_2 nanotubes. J. Mater. Sci. **44**, 4613–4616 (2009)
37. A.M. Abo, E.L. Ata, M.K.E. Nimr, S.M. Attia, D. El Kony, A.H. Al-Hammadi, Studies of AC electrical conductivity and initial magnetic permeability of rare-earth-substituted Li–Co ferrites. J. Magn. Magn. Mater. **297**(1), 33–43 (2006)
38. S.R. Elliott, Ac conduction in amorphous chalcogenide and pnictide semiconductors. J. Adv. Phys. **36**, 135–217 (1987)
39. A.S. Das, M. Roy, D. Biswas, R. Kundu, A. Acharya, D. Roy, S. Bhattacharya, Ac conductivity of transition metal oxide doped glassy nanocomposite systems: temperature and frequency dependency. Mater. Res. Express. **5**, 095201 (2018)

40. M.A. Darwish et al., Investigation of AC-measurements of epoxy/ferrite composites. Nanomater. **10**(3), 492 (2020). https://doi.org/10.3390/nano10030492
41. C.G. Koops, On the dispersion of resistivity and dielectric constant of some semiconductors at audio Frequencies. Phys. Rev. **83**, 121 (1951)
42. A. Rado'n, D. Lukowiec, M. Kremzer, J. Mikula, P. Wlodarczyk, Electrical conduction mechanism and dielectric properties of spherical shaped Fe_3O_4 nanoparticles synthesized by co-precipitation method. Materials. **11**, 735 (2018)
43. C.H. Rayssi, S. El Kossi, J. Dhahri, K. Khirouni, Frequency and temperature-dependence of dielectric permittivity and electric modulus studies of the solid solution $Ca_{0.85}Er_{0.1-}Ti_1-xCo_{4x/3}O_3$ ($0 \leq x \leq 0.1$). RSC Adv. **18**, 17139 (2018)
44. M. Yang et al., The preparation and dielectric properties of dielectric ceramic composites with controllable thermal expansion: $SrTiO_3$/ZrMg. J. Mater. Sci. Mater. Electron. **31**, 347 (2020)
45. A. Ashok, T. Somaiah, D. Ravinder, C. Venkateshwarlu, C. Reddy, K. Rao, M. Prasad, Electrical properties of cadmium substitution in nickel ferrites. World J. Condens. Matter Phys. **2**, 257–266 (2012)
46. D.Z. Chen, G.S. Wang, S. He, J. Liu, L. Guo, M.S. Cao, Controllable fabrication of mono-dispersed RGO–hematite nanocomposites and their enhanced wave absorption properties. J. Mater. Chem. A. **1**, 5996–6003 (2013)
47. H.J. Wu, L.D. Wang, S.L. Guo, Y.M. Wang, Z.Y. Shen, Electromagnetic and microwave-absorbing properties of highly ordered mesoporous carbon supported by gold nanoparticles. J. Mater. Chem. Phys. **133**, 965–970 (2012)
48. M. Zong, Y. Huang, Y. Zhao, X. Sun, C.H. Qu, D.D. Luo, J.B. Zheng, Facile preparation, high microwave absorption and microwave absorbing mechanism of RGO-Fe_3O_4 composites. J. RSC Adv. **45**, 23638–23648 (2013)
49. B. Wen, X.X. Wang, W.Q. Cao, H.L. Shi, M.M. Lu, G. Wang, H.B. Jin, W.Z. Wang, J. Yuan, M.S. Cao, Reduced graphene oxides: the thinnest and most lightweight materials with highly efficient microwave attenuation performances of the carbon world. J. Nanoscale. **6**, 5754–5761 (2014)
50. X.F. Zhang, X.L. Dong, H. Huang, B. Lv, J.P. Lei, C.J. Choi, Microstructure and microwave absorption properties of carbon-coated iron nanocapsules. J. Phys. D: Appl. Phys. **40**(17), 5383 (2007)
51. C.R. Bowen, A.W. Tavernor, J. Luo, R. Stevens, Microstructural, design of sensor materials using the core-shell concept. J. Eur. Ceram. Soc. **19**, 149–154 (1999)
52. D.C. Sinclair, T.B. Adams, F.D. Morrison, A.R. West, $CaCu_3Ti_4O_{12}$: One- step internal barrier layer capacitor. J. Appl. Phys. Lett. **80**, 2153–2155 (2002)
53. B. Yang, Y. Wang, P.-Y. Qian, Sensitivity and correlation of hypervariable regions in 16S rRNA genes in phylogenetic analysis. J. BMC Bioinformatics. **17**, 135 (2016). https://doi.org/10.1186/s12859-016-0992-y